
PHYSICS OF SEMICONDUCTOR
DEVICES

Ar Ion Irradiation Effects on the Characteristics of Ru|Pt|*n*-GaN Schottky Barrier Diodes

S. Kumar^a, V. Kumar Mariswamy^b, A. Kumar^c, A. Kandasami^c, A. Nimmala^d, S. V. S. Nageswara Rao^{d,e},
V. Rajagopal Reddy^f, and K. Sannathammegowda^{a,*}

^a Department of Studies in Physics, Manasagangotri, University of Mysore, Mysuru, 570006 India

^b Department of Physics, K L E Society's R L S Institute, Belagavi, 590001 India

^c Inter-University Accelerator Centre (IUAC), New Delhi, 110067 India

^d Centre for Advanced Studies in Electronics Science and Technology (CASEST), School of Physics, University of Hyderabad, Hyderabad, 500046 India

^e School of Physics, University of Hyderabad, Hyderabad, 500046 India

^f Department of Physics, Sri Venkateswara University Tirupati, Tirupati, 517502 India

*e-mail: sk@physics.uni-mysore.ac.in

Received July 28, 2020; revised July 28, 2020; accepted August 13, 2020

Abstract—The present study reports the effects of 650-keV Ar²⁺ ion irradiation on the structural, optical, and device characteristics of Ru|Pt|*n*-GaN Schottky barrier diodes (SBDs). Ion irradiation induces the broadening of the GaN X-ray diffraction peaks due to induced structural deformities. The photoluminescence spectroscopy intensity decreases with the increase in the fluence of ions. The recombination of charge carriers induced by the geometrical distortions, and the formation of defects states, shifts the peak positions to shorter wavelengths. The electrical characteristics of these devices exhibit significant changes due to modification at the interface and charge transport properties after Ar²⁺ ion irradiation. The charge-transport properties are affected by these deformities at higher fluences and attributed to the contributions of various current conduction mechanisms, including defect-assisted tunnelling and generation–recombination (G–R) currents along with thermionic emission.

Keywords: GaN SBDs, electrical parameters, ion irradiation, current conduction mechanisms

DOI: 10.1134/S1063782620120155

1. INTRODUCTION

Over the last few decades, GaN has become one of the fascinating compound semiconductor material for researchers in the field of device-fabrication technology due to its unique properties like large and direct energy bandgap, high melting point, high chemical resistance, and good thermal conductivity [1–4]. These properties make GaN a potential material of modern electronic devices for various applications such as amplifiers, dynamic switches, detectors, lasers, solar cells, transistors for terahertz plasma applications, diodes, including the devices that are reliable in radiation-rich environments [1–3, 5–9]. Low-energy ion irradiation is an effective technique for customizing materials and devices containing semiconductors. These ions, however, introduce electrically active defects that modify the properties of semiconductor material and thus alter the characteristics of the devices fabricated on it [6, 10–14]. Another advantage of low-energy ion irradiation is to test the reliability of the semiconductor devices under exposure to radiation at higher altitudes, e.g., for military

and space applications [9, 15–17] and their response in radiation environments at high energy physics experiments/accelerator facilities [18–22].

Therefore, studies of the influence of energetic ions on semiconductors and their device properties are primary research areas. In this context, we report the 650-keV Ar²⁺ ion-irradiation effects on the structural, optical, and electrical properties of Ru|Pt|*n*-GaN Schottky barrier diodes (SBDs) for various fluences to understand the current transport mechanism for its applications in different fields.

2. EXPERIMENTAL

In the present work, Ru(30 nm)|Pt(20 nm)|*n*-GaN SBDs were fabricated using a 2-μm thick *n*-GaN on the Al₂O₃ (C-plane) substrate. The comprehensive process of fabrication of Ru|Pt|*n*-GaN SBDs is described in detail in [23]. The Ru|Pt|*n*-GaN SBDs were irradiated by 650-keV Ar²⁺ ions using the low-energy ion-beam facility (LEIBF) housed at IUAC, New Delhi, India [24]. During irradiation, the beam

Table 1. TRIM Calculations for 650 keV Ar in Ru|Pt|*n*-GaN SBDs

Range <i>R</i> , Å	Displacement, /ion	Vacancies, /ion	NIEL up to <i>R</i> , MeV cm ² /g	LET, MeV cm ² /g
2962	5220	4977	1.35×10^3	2.24×10^3

current was 1 μ A (max), and the ion fluences ranged from 1×10^{13} to 1×10^{15} ions cm⁻². The X-ray diffraction (PANalytical: X'pert3 Powder) and photoluminescence (PL-Fluorolog, Xenon lamp, 450 W, Excitation: 350 nm, resolution: 0.3 nm) studies for pristine and irradiated samples were conducted at UGC-NRC School of Physics, Hyderabad. Room-temperature current–voltage (*I*–*V*) and capacitance–voltage (*C*–*V*) characterization were done using the semiconductor device analyzer (Agilent Technologies B1500A) at IUAC, New Delhi, India. All these electrical measurements were done as per MIL-STD 750 E standards [25].

3. RESULTS AND DISCUSSION

To understand the mechanism of energy loss, ion range, 650-keV argon ion-irradiation distribution, stopping range, non-ionizing energy loss (NIEL), linear energy transfer (LET), and ionization displacement profile were calculated (Table 1) using the stopping and range of ions in matter (SRIM) and transport of ions in matter (TRIM) simulations [26].

The methodologies followed for damage profile, LET, and NIEL calculations are similar to the details given in [27, 28]. Figure 1 displays the distribution of total ionization of target, and Fig. 2 displays the tar-

get's total displacements as a function of the device's thickness.

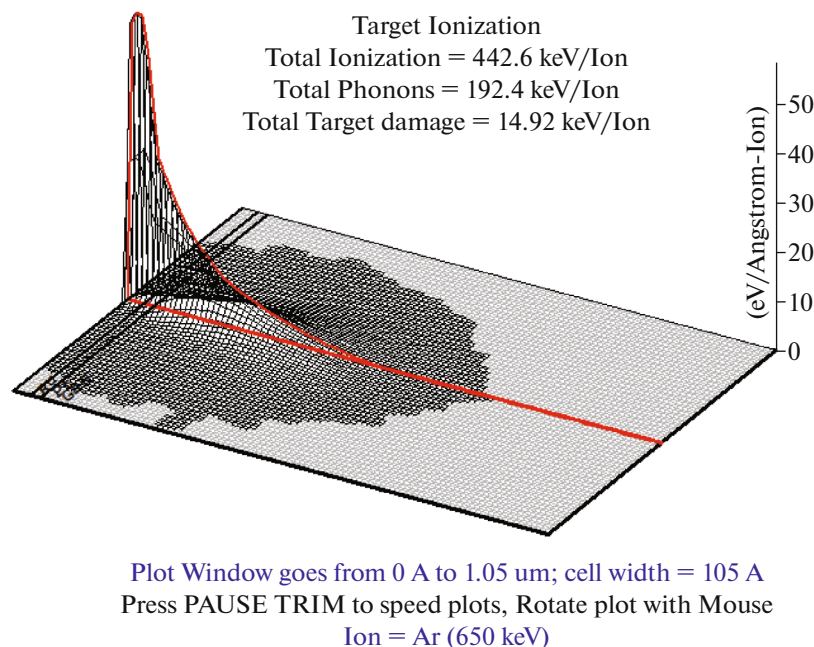
The distributions of ionization losses and displacement losses indicate the maximum damage at the metal–semiconductor (M–S) interface and decrease along with the depth of the semiconductor material. As a consequence, a large number of displacements/vacancies are commonly created due to displacement damage. In the same way, ionization damage produces electron–hole pairs. Higher LET values cause ionization and displacement damage. Table 2 lists the fluence-dependent total ionizing dose (TID) and displacement damage (*D_d*).

Room-temperature current–voltage *I*–*V* characteristics are shown in Fig. 3 for pristine and irradiated SBDs at different fluences: 1×10^{13} , 1×10^{14} , and 1×10^{15} ions cm⁻² of 650-keV Ar²⁺, respectively.

The thermionic emission (TE) property of the device is extracted from the *I*–*V* characteristics of the M–S contacts using the relation [29]:

$$I = AA^*T^2 \exp\left(-\frac{q\Phi_B}{kT}\right) \exp\left(-\frac{q(V - IR_S)}{nkT}\right), \quad (1)$$

where *A** is the effective Richardson constant, *A* is the diode area, *R_S* is the series resistance, *n* is the ideality

**Fig. 1.** The distribution of ionization losses in Ru|Pt|*n*-GaN SBDs for 650-keV Ar.

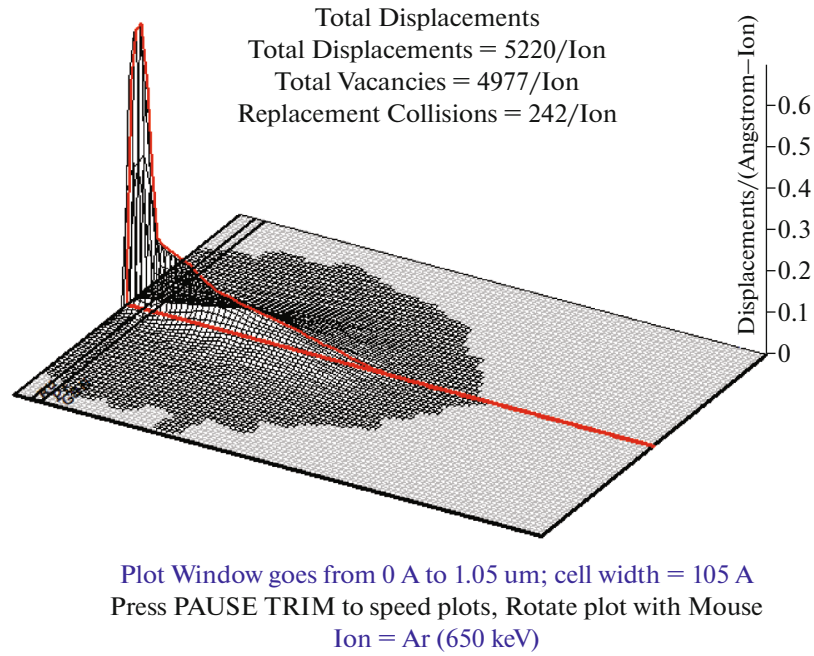


Fig. 2. The distribution of displacement losses in Ru|Pt|*n*-GaN SBDs for 650-keV Ar.

factor, ϕ_B is the Schottky barrier height, and the other terms have their usual meaning.

Employing the Cheung and Cheung's method [30], the electrical parameters R_S , n , and ϕ_B are calculated using the following relations:

$$\frac{dV}{d(\ln I)} = IR_S + n \left(\frac{kT}{q} \right), \quad (2)$$

$$H(I) = V - n \frac{kT}{q} \ln \left(\frac{I}{AA^* T^2} \right), \quad (3a)$$

$$H(I) = n\phi_B + IR_S. \quad (3b)$$

The extracted values of n , R_S , and ϕ_B from the above functions are given in Table 3.

The values of R_S obtained from Eq. (2) (Fig. 4a) and from Eq. (3b) (Fig. 4b) are nearly equal, which gives the uniformity of the method.

The Norde method [31] is used in the determination of large values of R_S of diodes, which involves the $F(V)$ function given as

$$F(V) = \frac{V}{2} - \frac{kT}{q} \ln \left(\frac{I(V)}{AA^* T^2} \right). \quad (4)$$

The R_S and ϕ_B are related as

$$R_S = \frac{kT}{qI_0}. \quad (5)$$

The minimum of the function $F(V)$ from the plot (Fig. 5) gives the values of $F(V_0)$, V_0 , which is related to minimal current I_0

$$\phi_B = F(V_0) + \frac{V_0}{2} - \frac{kT}{q}. \quad (6)$$

The values of n , R_S , and barrier ϕ_B extracted from Norde's method for different fluences of 650-keV Ar^{2+} ion irradiation are shown in Table 3.

The C - V measurements for pristine and irradiated Ru|Pt|*n*-GaN SBDs are done at a frequency of 1 MHz. Figure 6 demonstrates the I/C^2 reliance on the applied voltage of Ru|Pt|*n*-GaN SBDs.

From the slopes of linear fits to the experimental I/C^2 vs. V plots, the effective concentration of donor atoms N_d is calculated using relation [32]:

$$\frac{1}{C^2} = \frac{2}{A^2 q \epsilon_0 \epsilon_r N_d} \left(V_{bi} - \frac{kT}{q} - V \right), \quad (7)$$

where A is the area of the Schottky contact, N_d is the effective dopant concentration, V_{bi} is the built-in

Table 2. Dependence of TID and D_d on the fluence of 650-keV Ar in Ru|Pt|*n*-GaN SBDs

Fluence, ions cm^{-2}	TID, rad	D_d , rad
1×10^{13}	3.58×10^8	2.15×10^8
1×10^{14}	3.58×10^9	2.15×10^9
1×10^{15}	3.58×10^{10}	2.15×10^{10}

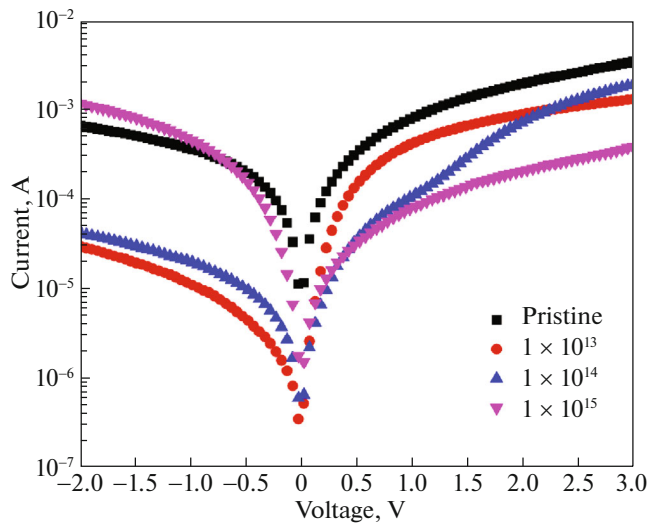


Fig. 3. I – V plots of pristine and irradiated Ru|Pt/ n -GaN SBDs for different fluences of 650-keV Ar^{2+} beam.

potential, and V is the applied reverse bias voltage, while the other terms have their usual meaning.

And the value of ϕ_B is calculated using the relation

$$\phi_B = V_{bi} + \frac{kT}{q} \ln \left(\frac{N_c}{N_d} \right), \quad (8)$$

where N_c is the density of states in the conduction band.

The extracted values of ϕ_B and N_d from C – V analysis are given in Table 4.

Tables 3 and 4 summarizes the values of n , R_S , and ϕ_B using the Cheung and Cheung method, Norde method, and capacitance–voltage measurement analysis. With higher fluences of 650-keV Ar^{2+} ion irradiation, R_S increases owing to the evolution of various defect levels in the band gap [33, 34]. Moreover, the increased value of R_S is due to the formation of a damaged layer in the semiconductor material along the ion path [18, 35]. The decrease in the ϕ_B after a fluence of 1×10^{13} ions cm^{-2} is a prominent reason of rise in the

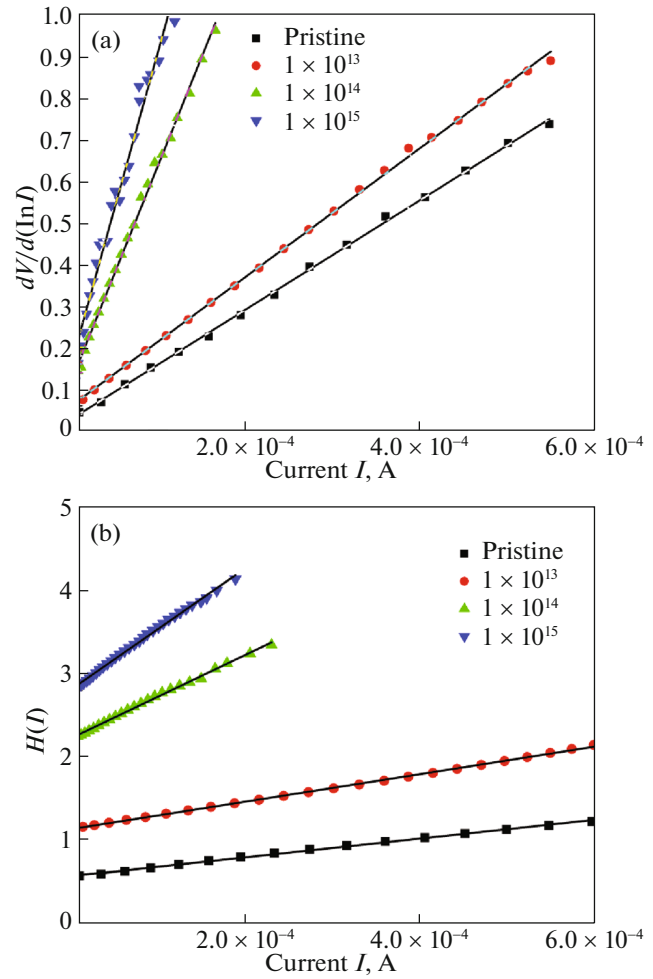


Fig. 4. (a) The $dV/d\ln I$ vs. I plot and (b) The $H(I)$ plot, of pristine and irradiated Ru|Pt/ n -GaN SBDs for different fluences of 650-keV Ar beam.

reverse saturation current. At lower fluence of 1×10^{13} ions cm^{-2} , the reverse current decreases nearly ten times as compared of pristine. It may be due to that after argon ion irradiation, more donors were introduced to the GaN surface. Whereas for highest fluence of 1×10^{15} ions cm^{-2} , the reverse current increases,

Table 3. The values of n , ϕ_B and R_S from Cheung and Cheung's method [23] and Norde method [24] of Ru|Pt/ n -GaN SBDs for different fluences of 650-keV Ar^{2+} beam

Fluence, ions cm^{-2}	Ideality factor n	Barrier height ϕ_B , eV		Series resistance R_S , k Ω			Reverse leakage current at -2 V, A
		$H(I)$	$F(V)$	$dV/d\ln I$	$H(I)$	$F(V)$	
Pristine	1.04	0.519	0.551	1.31	1.34	1.50	6.86×10^{-4}
1×10^{13}	1.89	0.603	0.642	1.67	1.64	1.86	3.10×10^{-5}
1×10^{14}	3.78	0.587	0.623	5.55	5.03	6.05	4.37×10^{-5}
1×10^{15}	5.01	0.558	0.606	7.98	7.45	11.5	1.24×10^{-3}

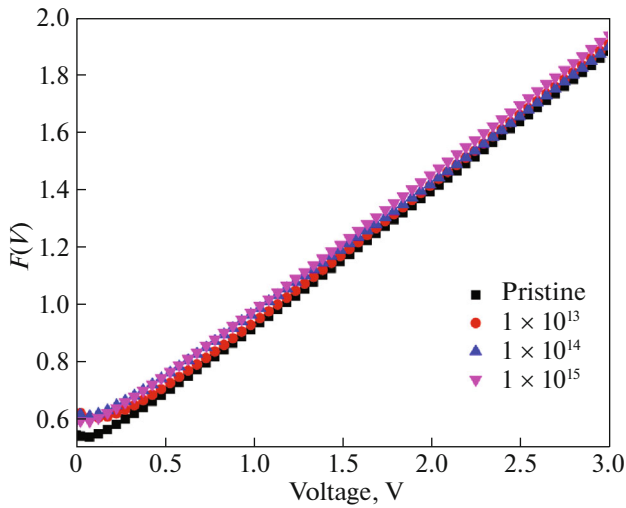


Fig. 5. The $F(V)$ plot of pristine and irradiated Ru|Pt/*n*-GaN SBDs for different fluences of 650-keV Ar²⁺ beam.

which may be due to the formation of deep energy levels in the middle of the forbidden gap that acts as generation–recombination (G–R) centers. The present study shows that the process of tunneling due to ion-induced defects has significantly altered the mechanism of charge transport in irradiated Ru|Pt/*n*-GaN SBDs [27, 28, 36]. After initial irradiation fluences, the value of n is observed to rise, which can be due to the increased contribution of tunnelling current. Whereas the drop in ϕ_B values after a fluence of 1×10^{13} ions cm⁻² is a prominent cause for the drastic increase in the reverse saturation current. TRIM simulations predict ionization and target damage for 650-keV Ar ion irradiation as 442.6 and 14.92 keV/ion. Due to the lower value of nuclear energy loss S_n , they cause less displacement damage than ionization across the interface. This additionally prompts a noteworthy decrease in the values of ϕ_B . Whereas with higher fluence, several non-trivial effects can be observed because of defects caused by avalanche overlapping [14]. The elastic collision produces defects such as vacancies and interstitials in the semiconductor material. The combination or agglomeration of these defects leads to complex and stable defect structures [14]. These defects have associated deep levels within the semiconductor band gap and act as traps for free carriers, which reduces their concentration. The Schottky diode's decrease in capacitance means an increase in the depletion width of the semiconductor [14].

In addition, I – V attributes were drawn in the logarithmic scale for the pristine and 650-keV Ar²⁺ ion irradiated SBDs to explore the dominant current conduction mechanism in the forward-bias region, as shown in Fig. 7.

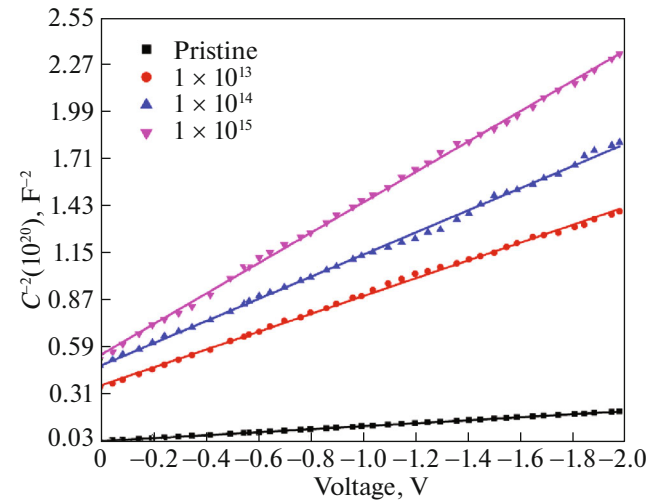


Fig. 6. C^{-2} vs. V plot of pristine and irradiated Ru|Pt/*n*-GaN SBDs for different fluences of 650-keV Ar²⁺ beam.

The current in the region with forward bias ($\log I$ vs. $\log V$ plots) is given as [14, 37]

$$I \propto V^p, \quad (9)$$

where p is the slope of different linear regions and shows the various current conduction mechanisms of the forward-biased Ru|Pt/*n*-GaN SBDs.

$\log I$ vs. $\log V$ plots (Fig. 7) are found to have three (I, II, and III) linear regions with different slopes shown in Table 5.

These linear regions demonstrate the existence of fluctuating conduction mechanisms. For pristine, the slope value for Region I is about one corresponding to the ohmic behavior, which may be due to the expansion of thermally-produced carriers. Whereas, the slope value close to 2 in irradiated samples demonstrates the space-charge-limited current with discrete trapping levels [38, 39].

Figure 8 shows the results of the reverse current conduction in SBDs after 650-keV Ar²⁺ ion irradiation to classify the major current transport mechanism at M–S junction between Poole–Frenkel emission (PFE) or Schottky emission (SE) mechanism [40, 41].

Table 4. The values of ϕ_B and N_d of Ru|Pt/*n*-GaN SBDs for different fluences of 650-keV Ar²⁺ beam

Fluence, ions cm ⁻²	ϕ_B , eV	Effective N_d , 10 ¹⁶ cm ⁻³
Pristine	0.652	13.2
1×10^{13}	0.803	1.81
1×10^{14}	0.762	1.06
1×10^{15}	0.698	1.02

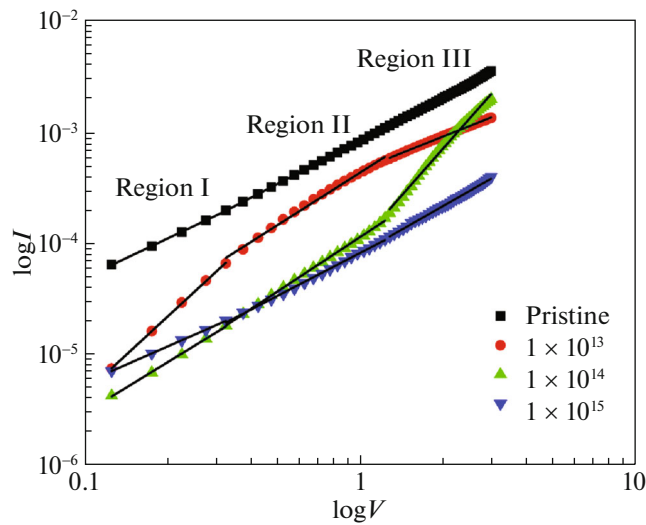


Fig. 7. The $\log V$ vs. $\log I$ plot of pristine and irradiated Ru|Pt/n-GaN SBDs for different fluences of 650-keV Ar^{2+} beam.

When dominated by PFE mechanism, the reverse current is given by

$$I_R \propto I_0 \exp\left(\frac{\beta_{\text{PF}} V^{1/2}}{kTd^{1/2}}\right), \quad (10)$$

and for SE mechanism, current is given by

$$I_R \propto AA^* \exp\left(-\frac{\Phi_B}{kT}\right) \exp\left(\frac{\beta_{\text{SE}} V^{1/2}}{kTd^{1/2}}\right). \quad (11)$$

The theoretical β_{PF} and β_{SE} values are given by

$$\beta_{\text{PF}} = 2\beta_{\text{SE}} = \left(\frac{q^2}{\pi\epsilon_0\epsilon_r}\right)^{1/2}. \quad (12)$$

For Ru|Pt/n-GaN SBDs, the theoretical values of field-lowering coefficients are estimated to be $2.54 \times 10^{-5} \text{ eV m}^{1/2} \text{ V}^{-1/2}$ (β_{PF}) and $1.27 \times 10^{-5} \text{ eV m}^{1/2} \text{ V}^{-1/2}$ (β_{SE}), respectively.

The findings has shown that the reverse current conduction mechanism is mainly due to SE in

Table 5. The slope from the $\log V$ vs. $\log I$ plot of Ru|Pt/n-GaN SBDs for different fluences of 650-keV Ar^{2+} beam

Fluence, ions cm^{-2}	Slope values		
	region I	region II	region III
Pristine	1.18	1.29	1.22
1×10^{13}	2.30	1.58	0.98
1×10^{14}	1.52	1.64	2.81
1×10^{15}	1.09	1.29	1.42

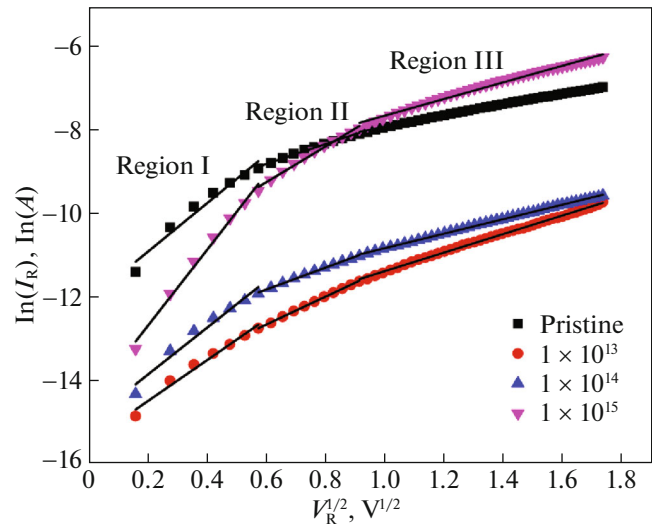


Fig. 8. The I_R vs. $V^{1/2}$ plot of pristine and irradiated Ru|Pt/n-GaN SBDs for different fluences of 650-keV Ar^{2+} beam.

Region III, and also increased at higher fluences (Table 6).

It can be concluded from the aforementioned conduction mechanism curves that the modifications for the Ru|Pt/n-GaN SBDs are mainly due to the high density of structural deformities or trap levels caused by 650-keV Ar^{2+} ion irradiation [37]. It confirms that the trapping/detrapping of charge carriers takes place predominantly at diode M–S interfaces [14, 42].

Characterizations of the room-temperature photoluminescence (PL) have been investigated for the optically dynamic interface imperfection states and their advancement during 650-keV Ar^{2+} ion irradiation. Figure 9 displays the deconvoluted PL spectrum of the pristine sample (inset) and the comparative PL spectrum of pristine and 650-keV Ar^{2+} ion irradiated Ru|Pt/n-GaN SBDs for different fluences.

The deconvoluted PL spectrum of pre-radiated pristine sample reveals emission peaks at near UV

Table 6. The experimental values of β_{PF} and β_{SE} of Ru|Pt/n-GaN for different fluences of 650-keV Ar^{2+} beam

Fluence, ions cm^{-2}	Experimental values, $10^{-5} \text{ eV m}^{1/2} \text{ V}^{-1/2}$					
	region I		region II		region III	
	β_{PF}	β_{SE}	β_{PF}	β_{SE}	β_{PF}	β_{SE}
Pristine	3.39	1.69	1.39	0.069	0.077	0.038
1×10^{13}	2.86	1.43	1.94	0.097	1.30	0.065
1×10^{14}	3.28	1.64	1.53	0.077	1.10	0.055
1×10^{15}	5.32	2.61	2.50	1.25	0.013	0.012

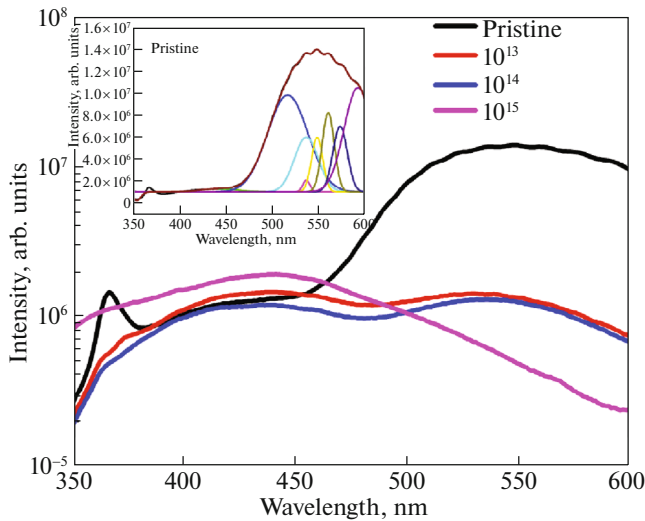


Fig. 9. The PL spectra of pristine and irradiated Ru|Pt/*n*-GaN SBDs for different fluences of 650 keV Ar²⁺ beam (inset: deconvoluted PL spectrum of pre-irradiated pristine sample).

(352.8 nm), blue luminescence {BL (431.8 nm)}, cyan luminescence {CL (505.8 nm)}, green luminescence {GL (531.2 nm)}, and yellow luminescence {YL (572.9 nm)} [43, 44] as shown in Fig. 9 inset. These peaks may be due to Ga|N vacancies or deep-level impurities in the pristine sample [39, 40]. GL and YL intensities decrease with 650-keV Ar²⁺ ion irradiation, and its shifts to shorter wavelengths may be due to the charge carrier's recombination, induced geometrical distortions, and formation of defects state, which serve as recombination traps [14, 45, 46]. In addition, the evolution of BL (440.9, 446.9, and 463.7 nm) with the highest fluence (1×10^{-15} ions cm⁻²) may be due to the further defect formations [14, 47, 48]. These donor-nitrogen vacancies transition indicates that after argon ion irradiation, more donors were introduced to the GaN surface. The intensity of YL decreases for high fluence, which contributes to the introduction of many traps for gallium vacancies [14, 47, 48]. The results of PL are consistent with *I*-*V* and *C*-*V* data, reconfirming the observation that donor-

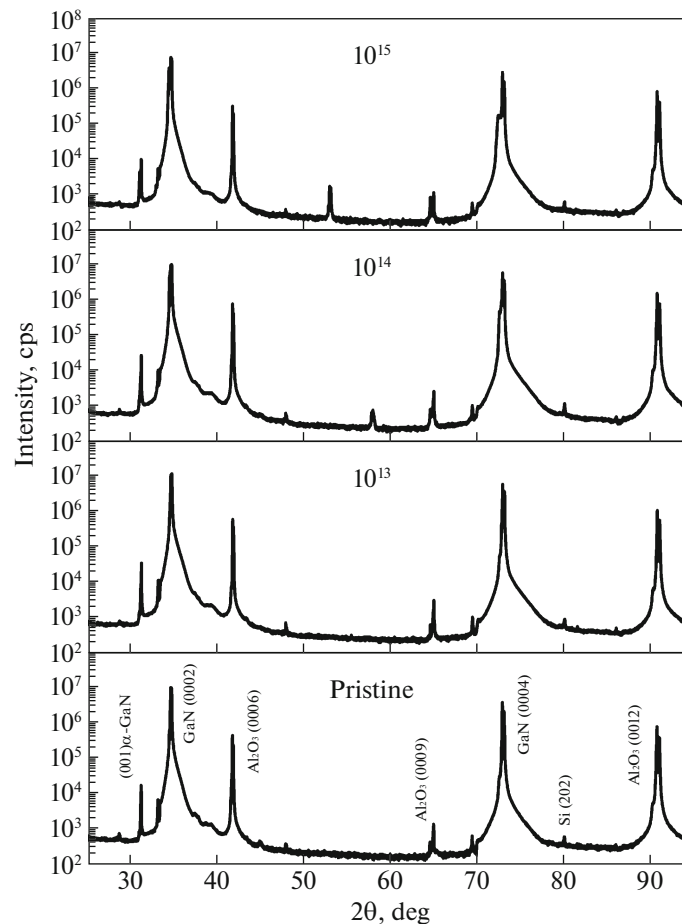


Fig. 10. The XRD pattern of pristine and irradiated Ru|Pt/*n*-GaN SBDs for different fluences of 650-keV Ar²⁺ beam.

nitrogen vacancies were introduced to the GaN surface at lower fluences.

In order to investigate structural modifications at the interface of Ru|Pt/*n*-GaN SBDs due to 650-keV Ar²⁺ ion irradiation, XRD peaks studies (Fig. 10) were performed, spanning 2 θ angles from 25° to 95°.

There are distinct diffraction peaks of GaN (0002), GaN (0004), GaN (0001), Al₂O₃ (0006), GaN (0003), Al₂O₃ (0009), and Si (202) [48, 49] in the pristine sample. After 650-keV Ar²⁺ ion irradiation, peaks of GaN (0002) and GaN (0004) have been found to be broadened, and it can be due to formations of structural damage and associated strains [49, 50].

4. CONCLUSIONS

Room-temperature studies on the current transport properties of Ru|Pt/*n*-GaN SBDs were investigated for pristine and irradiated SBDs for different fluences; 1×10^{13} , 1×10^{14} , and 1×10^{15} ions cm⁻² of 650 keV Ar²⁺. The electrical parameters *n*, *R_s*, and ϕ_B were obtained from the thermionic emission (TE) model, Norde's method, and *C-V* technique. The value of *n* increases with higher fluences, due to multiple transport mechanisms activation. The value of ϕ_B increases with a fluence of 1×10^{13} ions cm⁻² and decreases further at higher fluences. The value of *R_s* increases for higher fluences, which may be due to contributions from various current transport mechanisms, including defect-assisted tunneling (DAT) and G-R along with TE. Ion irradiation mainly reduces carrier mobility and carrier concentration and enhances the *R_s*, as can also be seen in the analysis. As confirmation by SRIM and TRIM calculations, Ar ion irradiation has introduced a large number of displacements and vacancies and these defects increase the *R_s* by reducing carriers concentration. Moreover, ion irradiation shows the significant contribution of tunneling currents as seen from higher forward currents than the low reverse currents up to a fluence of 1×10^{13} ions cm⁻². This implies that due to high nuclear energy losses more displacement damage is caused in the lattice, leading to a huge contribution from DAT currents.

The XRD pattern shows that ion irradiation induces broadening of the peaks of GaN (0002), and GaN (0004) because of structural damage. The intensities of green and yellow emissions decrease with ion irradiation and also shift towards shorter wavelengths because of the recombination of chargers, instigated geometrical bends, and arrangement of imperfections state, which enhances the recombination traps.

ACKNOWLEDGMENTS

The authors are thankful to the staff and technicians at IUAC, New Delhi, India, for providing access to Low

Energy Beam Ion irradiation, *I-V*, and *C-V* measurement facilities. The authors are also grateful to the Central facility for nanotechnology (CFN), and the School of Physics (UGC-NRC), University of Hyderabad, for providing access to necessary experimental facilities.

CONFLICT OF INTEREST

There are no conflicts to declare.

REFERENCES

1. Y. S. Katharria, S. Kumar, P. S. Lakshmy, D. Kanjilal, and A. T. Sharma, *J. Appl. Phys.* **102**, 044301 (2007).
2. W. Monch, *Rep. Prog. Phys.* **53**, 221 (1990).
3. A. Kumar, T. Kumar, A. Hähnel, D. Kanjilal, and R. Singh, *Appl. Phys. Lett.* **104**, 033507 (2014).
4. A. Kumar, T. Singh, M. Kumar, and R. Singh, *Curr. Appl. Phys.* **14**, 491 (2014).
5. C. Sharma, A. K. Visvkarma, R. Laishram, A. Kumar, D. S. Rawal, S. Vinayak, and R. Singh, *Microelectron. Reliab.* **105**, 113565 (2020).
6. A. Kumar, A. Hähnel, D. Kanjilal, and R. Singh, *Appl. Phys. Lett.* **101**, 153508 (2012).
7. D. W. Runtton, B. Trabert, J. B. Shealy, and R. Veturly, *IEEE Microwave Mag.* **14**, 82 (2013).
8. H. Amano, Y. Baines, E. Beam, M. Borga, T. Bouchet, P. R. Chalker, M. Charles, K. J. Chen, N. Chowdhury, R. Chu, C. de Santi, M. M. de Souza, S. Decoutere, L. di Cioccio, B. Eckardt, et al., *J. Phys. D: Appl. Phys.* **51**, 163001 (2018).
9. S. O. Kucheyev, J. S. Williams, and S. J. Pearton, *Mater. Sci. Eng. R* **33**, 51 (2001).
10. A. Kumar, J. Dhillon, S. Verma, P. Kumar, K. Asokan, and D. Kanjilal, *Semicond. Sci. Technol.* **33**, 085008 (2018).
11. T. Mohanty, S. Dhounsi, P. Kumar, A. Tripathi, and D. Kanjilal, *Surf. Coat. Technol.* **203**, 2410 (2009).
12. K. Iniewski, *Nano-Semiconductors: Devices and Technology* (CRC, Boca Raton, FL, 2011).
13. J. L. Benton, S. Libertino, and P. Kringhøj, *J. Appl. Phys.* **82**, 120 (1997).
14. S. Kumar, X. Zhang, V. K. Mariswamy, V. R. Reddy, A. Kandasami, A. Nimmala, S. V. S. N. Rao, J. Tang, S. Ramakrishna, and K. Sannathammegowda, *Materials* **13**, 1299 (2020).
15. S. Libertino, S. Coffa, and J. L. Benton, *Phys. Rev. B* **63**, 195206 (2001).
16. S. Fatima, J. Wong-Leung, J. Fitz Gerald, and C. Jagadish, *Appl. Phys. Lett.* **72**, 3044 (1998).
17. B. G. Svensson, C. Jagadish, A. Hallén, and J. Lalita, *Phys. Rev. B* **55**, 10498 (1997).
18. A. Kumar, R. Singh, P. Kumar, U. B. Singh, K. Asokan, P. A. Karaseov, A. I. Titov, and D. Kanjilal, *J. Appl. Phys.* **123**, 161539 (2018).
19. P. Bogdanski, P. Mary, and M. Toulemonde, *Nucl. Instrum. Methods Phys. Res., Sect. B* **62**, 388 (1992).
20. P. K. Giri and Y. N. Mohapatra, *J. Appl. Phys.* **84**, 1901 (1998).

21. P. Kodali, M. Hawley, K. C. Walter, K. Hubbard, N. Yu, J. R. Tesmer, T. E. Levine, and M. Nastasi, *Wear* **205**, 144 (1997).
22. S. O. Kucheyev, J. S. Williams, C. Jagadish, J. Zou, and G. Li, *Phys. Rev. B* **62**, 7510 (2000).
23. N. N. K. Reddy and V. R. Reddy, *Bull. Mater. Sci.* **35**, 53 (2012).
24. T. Sairam, P. Bhatt, A. Kumar, H. Kumar, and C. P. Safvan, *Phys. Plasmas* **22**, 113503 (2015).
25. Anon Test Method Standard for Semiconductor Devices, MIL-STD-750E (2007).
26. R. E. Stoller, M. B. Toloczko, G. S. Was, A. G. Certain, S. Dwaraknath, and F. A. Garner, *Nucl. Instrum. Methods Phys. Res., Sect. B* **310**, 75 (2013).
27. M. V. Kumar, S. Verma, V. Shobha, B. Jayashree, D. Kanjilal, and S. Krishnaveni, *J. Mater. Sci. Res.* **3**, 24 (2014).
28. M. V. Kumar, S. Verma, K. Asokan, V. Shobha, S. P. Karanth, and S. Krishnaveni, *ECS J. Solid State Sci. Technol.* **5**, P384 (2016).
29. A. B. Garg, R. Mittal, and R. Mukhopadhyay, *AIP Conf. Proc.* **1349**, 1 (2011).
30. S. K. Cheung and N. W. Cheung, *Appl. Phys. Lett.* **49**, 85 (1986).
31. H. Norde, *J. Appl. Phys.* **50**, 5052 (1979).
32. P. Hacke, T. Detchprohm, K. Hiramatsu, and N. Sawaki, *Appl. Phys. Lett.* **63**, 2676 (1993).
33. S. A. Goodman, F. D. Aurret, and W. E. Meyer, *Nucl. Instrum. Methods Phys. Res., Sect. B* **90**, 349 (1994).
34. A. P. Karmarkar, B. Jun, D. M. Fleetwood, R. D. Schrimpf, R. A. Weller, B. D. White, L. J. Brillson, and U. K. Mishra, *IEEE Trans. Nucl. Sci.* **51**, 3801 (2004).
35. D. J. Mazey, R. S. Nelson, and R. S. Barnes, *Philos. Mag.* **17**, 1145 (1968).
36. V. R. Reddy and N. N. K. Reddy, *Superlatt. Microstruct.* **52**, 484 (2012).
37. N. Manikanthababu, S. Vajandar, N. Arun, A. P. Pathak, K. Asokan, T. Osipowicz, T. Basu, and S. V. S. Nageswara Rao, *Appl. Phys. Lett.* **112**, 131601 (2018).
38. S. K. Gautam, J. Singh, R. G. Singh, N. Gautam, P. Trivedi, and F. Singh, *IEEE Trans. Electron. Dev.* **66**, 1475 (2019).
39. S. Kumar, M. V. Kumar, and S. Krishnaveni, *Semiconductors* **54**, 169 (2020).
40. T. S. Shafai and T. D. Anthopoulos, *Thin Solid Films* **398**, 361 (2001).
41. A. S. Riad, *Phys. B* **270**, 148 (1999).
42. M. Prokesch, in *Solid-State Radiation Detectors: Technology and Applications* (CRC, Boca Raton, 2015), p. 17.
43. M. Nikl, *Phys. Status Solidi A* **178**, 595 (2000).
44. R. Armitage, Q. Yang, and E. R. Weber, *J. Appl. Phys.* **97**, 073524 (2005).
45. G. Santana, O. De Melo, J. Aguilar-Hernández, R. Mendoza-Pérez, B. Monroy, A. Escamilla-Esquivel, M. López-López, F. de Moure, L. Hernández, and G. Contreras-Puente, *Materials* **6**, 1050 (2013).
46. A. Ionascut-Nedelcescu, C. Carlone, A. Houdayer, H. J. von Bardeleben, J. Cantin, and S. Raymond, *IEEE Trans. Nucl. Sci.* **49**, 2733 (2002).
47. M. Thaik, U. Hömmerich, R. N. Schwartz, R. G. Wilson, and J. M. Zavada, *Appl. Phys. Lett.* **71**, 2641 (1997).
48. Z. Sitar, M. J. Paisley, B. Yan, J. Ruan, W. J. Choyke, and R. F. Davis, *J. Vac. Sci. Technol. B* **8**, 316 (1990).
49. Y.-W. Lee, M. S. P. Reddy, B.-M. Kim, and C. Park, *Opt. Mater.* **81**, 109 (2018).
50. F. Ben Nasr, H. Guermazi, and S. Guermazi, *Eur. Phys. J. Plus* **131**, 195 (2016).